Manipulation by magnetic frustration in ferrotoroidal spin chains via curvature and torsion

Oleksandr V. Pylypovskyi [1,2,*] Enrico Di Benedetto [1,3] Carmine Ortix [4] and Denys Makarov [1,†]
[1]Helmholtz-Zentrum Dresden-Rossendorf e.V., Institute of Ion Beam Physics and Materials Research, 01328 Dresden, Germany
[2]Kyiv Academic University, Kyiv 03142, Ukraine
[3]Dipartimento di Fisica e Chimica "E. Segrè", Università degli Studi di Palermo, 90123 Palermo, Italy
[4]Dipartimento di Fisica "E. R. Caianiello", Università di Salerno, IT-84084 Fisciano (SA), Italy

(Received 30 August 2024; accepted 23 December 2024; published 23 January 2025)

Geometric effects in curvilinear nanomagnets can enable chiral, anisotropic, and even magnetoelectric responses. Here, we study the effects of magnetic frustration in curvilinear (quasi-)one-dimensional magnets represented by spin chains arranged along closed space curves of constant torsion. Considering the cases of easy- and hard-axis anisotropy in ferro- and antiferromagnetic samples, we determine their ground states and analyze the related magnetoelectric multipoles. A constant torsion along the chain results in alternating regions of high and low curvature, facilitating the spin spiral state perturbed by the (anti)periodic boundary conditions on the magnetic order parameter. While easy-axis ferromagnetic chains develop a purely toroidal configuration with the magnetic toroidal moment oriented along the geometry symmetry axis, hard-axis antiferromagnetic chains support multiple magnetic toroidal domains. Our findings suggest that tailoring curvature and torsion of a spin chain enables a different physical mechanism for magnetic frustration, which can be observed in the inhomogeneity of the magnetic order parameter and in the local ferrotoroidal responses.

DOI: 10.1103/PhysRevResearch.7.013088

I. INTRODUCTION

Nontrivial geometry of low-dimensional objects such as wires, ribbons, and shells emerged as an effective way to modify their responses to external stimuli [1]. These phenomena are intensively explored for a broad range of condensed matter systems, including two-dimensional materials [2] and topological insulators and semimetals [3], in addition to more established curvilinear semiconductors [1], superconductors [4,5], and magnetic materials [6–8]. Very recently, the geometry of curvilinear magnetic wires with intrinsic Dzyaloshinskii-Moriya interaction (DMI) was explored to realize artificial systems characterized by magnetoelectric multipoles [9]. Indeed, geometric effects can result in a magnetically induced breaking of inversion symmetry and consequently to the appearance of magnetoelectic monopoles, as well as toroidal and quadrupole moments. Materials with finite magnetoelectric multipole moments are of major fundamental interest in the study of magnetoelectric coupling phenomena [10]. Typically, magnetoelectric monopoles, as well as toroidal and quadrupolar moments, in materials are realized at the level of crystal structure. The use of geometry-induced breaking of inversion symmetry can extend the number of magnetoelectric materials since it can virtually equip any appropriately curved magnetic material with higher-order magnetoelectric multipoles.

Here, we study magnetic states in spin chains following space curves of constant torsion. For completeness, we address the cases of ferro- and antiferromagnetic coupling in the spin chain. The geometries studied here belong to the family of spherical epicycles, which are characterized by the three- and fourfold symmetry axis only with three and four number of knots without self-intersections, respectively. These systems highlight the role of a finite torsion on the physical properties of three-dimensional (3D) nanoarchitectures. We describe the ground states in samples with easy- and hard-axis magnetic anisotropy including the case of odd number of spins in the chain, which leads to magnetic frustration. The equilibrium magnetic textures are determined by the competition between the strength of anisotropy, geometry-driven DMI, and (anti)periodic boundary conditions. The latter depends on the number of knots and spins in the case of the antiferromagnetic (AFM) exchange coupling. We show that in this case, the magnetic frustration of the ground state (the total winding phase of the order parameter is an odd or even multiple of π) is dependent not only on the number of spins, but also on the number of knots in the geometry. The magnetic texture in epicycles breaks the space-inversion symmetry and allows for higher-order magnetoelectric multipoles. In particular, while spin chains with ferromagnetic coupling and easy-axis anisotropy are characterized by a macrotoroidal moment, hard-axis systems can be split into multiple toroidal domains.

The paper is organized as follows. In Sec. II, we introduce curvature effects in magnetic systems. In Sec. III, the

*Contact author: o.pylypovskyi@hzdr.de
†Contact author: d.makarov@hzdr.de

geometry, spin-lattice model, and the respective nonlinear σ model are introduced. In Sec. IV, we describe ground states of closed ferromagnetic and antiferromagnetic spin chains analyzing cases of the easy- and hard-axis anisotropy, magnetically soft chains with dominating dipolar interaction, and chains with antiferromagnetic exchange and odd number of spins. In Sec. V, the static ferrotoroidal ordering in these systems is described. In Sec. VI, we summarize the identified magnetic states and describe the interplay between magnetic frustration originating either purely from the sample geometry (distribution of curvature and torsion) or due to the odd number of spins, and provide the summary in Sec. VII. In Appendix A, details of the construction of the epicycle geometry are provided. Appendix B describes boundary conditions in the σ model for chains with antiferromagnetic exchange and odd number of spins. In Appendixes C and D, we provide the equations of state and describe spin-lattice simulations, respectively.

II. CURVATURE EFFECTS IN MAGNETISM

In magnetism, the static effects of geometry are usually related to the presence of geometry-tracking interactions such as magnetostatics, interfacial phenomena, or DMI. Then, breaking of space-inversion symmetry due to the curved shape of the sample is mapped onto the behavior of the magnetic vector order parameter.

Strong attention has been paid to high-symmetry samples, with a particular focus on (quasi)-1D systems [8]. Thin bent nanowires or spin chains with ferro- or antiferromagnetic exchange are convenient objects of study that capture the hallmarks of more complex geometries. Such chains are characterized by curvature κ and torsion τ, two geometric quantities describing in-plane bends and screw deformation of the given space curve, respectively. Prototypical examples of such systems are represented by helices, characterized by constant κ and τ, which can be readily realized in experiments [11–16]. On one hand, thin helical ferromagnetic (FM) nanowires have the ground state tilted from the tangential direction due to the geometry-driven anisotropy stemming from exchange interaction [17–19] and support chiral domain walls [18]. The selection of κ and τ can be used for modulating the magnetic states in intrinsically chiral materials [20] or tailoring the properties of heterostructures with piezoelectric [21] or superconducting [22] matrices. On the other hand, antiferromagnetic (AFM) helical systems show a broad range of transport phenomena, which can be tailored by geometric parameters [23–25]. At present, the analysis of geometric effects is mainly limited to planar geometries ($\tau = 0$) with a ringlike shape ($\kappa = \text{const}$) [26,27] or where curvature gradients act as pinning potentials for the noncollinear FM and AFM magnetic textures [28–31]. In geometries following space curves, the gradients of κ and τ in 3D nanostructures result in the self-propelling of domain walls [32–35].

Inversion symmetry breaking in curvilinear magnetic systems can lead to a broader range of phenomena, such as geometry-induced magnetoelectricity due to the possibility to support nonvanishing magnetoelectric multipoles [9]. This fundamental knowledge is of relevance for the analysis of the response of a broad class of single-molecule magnets in a toroidal ground state [36–38].

In addition to extensively discussed open-end systems such as helices, it is insightful to focus on closed-space curves, as they allow one to discuss the effects in terms of the topological properties of the sample geometry. In this respect, the correlation between the topology of the geometry and the topology of the magnetic texture in effectively 1D systems can be established [39].

Furthermore, much attention is usually dedicated to the effects of curvature, while torsion is usually considered as a secondary parameter. In strictly 1D systems, torsion reveals itself only in the presence of a finite curvature [40]. Hence, the impact of torsion on the behavior of curvilinear magnetic systems is not yet well studied. This seems to be a severe limitation, especially considering that the case of nonzero torsion distinguishes a planar curved wire from a truly 3D curved wire. To facilitate this understanding, in this manuscript we focus on closed-space curves with constant torsion.

III. THE MODEL

A. Geometry

We consider spin chains arranged along a space curve $\boldsymbol{\gamma}(s) \in \mathcal{C}^3(\mathbb{R})$ characterized by a constant torsion $\tau = [(\partial_s\boldsymbol{\gamma} \times \partial_s^2\boldsymbol{\gamma}) \cdot \partial_s^3\boldsymbol{\gamma}]/|\partial_s^2\boldsymbol{\gamma}|^2$, where s is the arc length [Fig. 1(a)]. Exemplary mathematical approaches to design such geometries include Bäcklund transformation [41], building curves dual to the curves of constant curvature $\kappa = |\partial_s\boldsymbol{\gamma} \times \partial_s^2\boldsymbol{\gamma}|/|\partial_s\boldsymbol{\gamma}|^3$ [42], and transformation of spherical curves $\boldsymbol{\beta}$ [43],

$$\boldsymbol{\gamma}(s) = \frac{1}{\tau}\int_0^s \left(\boldsymbol{\beta} \times \frac{d\boldsymbol{\beta}}{d\tilde{s}}\right) d\tilde{s}. \tag{1}$$

Here, $\boldsymbol{\beta}$ plays a role of the binormal vector $\boldsymbol{e}_\mathrm{B}$ for $\boldsymbol{\gamma}$. It has positive geodesic curvature and possesses zero Peano direction [44]. The latter implies the presence of an inversion center for certain projections of the curve. In this work, we use the approach (1) and generate spherical curves following the method by Bates and Melko [45]. We chose two-parametric epicycles $\boldsymbol{\beta}_p^r$, where r counts the number of traces of a unit sphere following the epicycle, and p is a winding number equal by absolute value to the number of knots on the curve; see Appendix A for details. The associated curve $\boldsymbol{\gamma}_p^r$ inherits the number of knots $|p|$. The transformation (1) lifts the presence of self-intersections (see example of $\boldsymbol{\gamma}_{-3}^1$), which is superimposed with an AFM texture in Fig. 1(a). The resulting symmetry of the curve is the $|p|$-fold rotation axis $C_{|p|}$. In the following, we introduce the laboratory Cartesian reference frame in such a way as to have the $\hat{\boldsymbol{z}}$ axis along the symmetry axis of the epicycle.

As an example, we consider the case of $\boldsymbol{\gamma}_{-3}^1$. According to its C_3 symmetry, the curvature of $\boldsymbol{\gamma}_{-3}^1$ exhibits three peaks corresponding to the number of knots of the generating curve [Fig. 1(b)]. The shape of $\kappa(s)$ in the vicinity of extrema can be well approximated by a Cauchy-Lorentz function (Appendix A). This is valid for any $\boldsymbol{\gamma}_p^1$.

Following the Frenet-Serret approach, the local reference frame on $\boldsymbol{\gamma}$ is determined by the tangential (T) $\boldsymbol{e}_\mathrm{T} = \partial_s\boldsymbol{\gamma}$, normal (N) $\boldsymbol{e}_\mathrm{N} = (\partial_s^2\boldsymbol{\gamma})/\kappa$, and binormal (B) $\boldsymbol{e}_\mathrm{B} = \boldsymbol{e}_\mathrm{T} \times \boldsymbol{e}_\mathrm{N}$

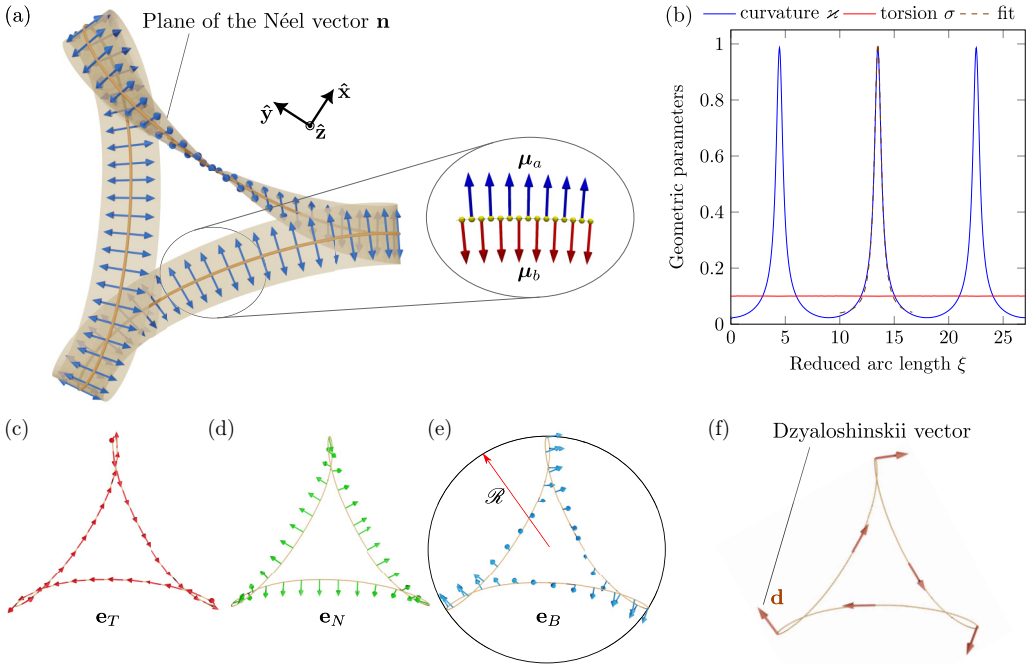

FIG. 1. (a) An antiferromagnetic (AFM) spin chain whose shape follows the epicycle $\boldsymbol{\gamma}^1_{-3}$. The direction of the Néel vector $\boldsymbol{n}$ for each dimer is shown in blue, whereas the envelope surface resulting from the continuous variation of the $\boldsymbol{n}$ vector along the curve is drawn in light yellow. In the inset, schematics of the two magnetic sublattices $\boldsymbol{\mu}_a$ and $\boldsymbol{\mu}_b$ are shown. (b) Reduced curvature $\varkappa$ for torsion $\sigma = 0.1$. Each peak of the dimensionless curvature κ can be well fitted with a Lorentzian profile, shown for comparison with an orange dashed line. (c)–(e) TNB frame in real space for the geometry shown in panel (a). The red arrow indicates the radius of the circumscribed ring $\mathscr{R}$. (f) The direction of the Dzyaloshinskii vector $\boldsymbol{d}$ in some representative points along the epicycle. Arrows are not to scale.

directions, respectively Figs. 1(c)–1(e). The direction of $\boldsymbol{e}_{\rm B}$ shown in Fig. 1(e) has clear evidence of the broken symmetry at each knot. A curve generated by Eq. (1) can be circumscribed in a circle of radius $\mathscr{R} = C/\tau$, with a constant C being dependent on $\boldsymbol{\beta}$ [Figs. 1(e) and 1(f)]. In contrast to plane rings whose characteristic size is determined by κ, the characteristic size $\mathscr{R}$ of $\boldsymbol{\gamma}$ grows with smaller torsion. In the following, we focus on the curves $\boldsymbol{\gamma}^1_{-3}$ and $\boldsymbol{\gamma}^1_{-4}$.

B. Spin-lattice Hamiltonian

In the magnetic Hamiltonian of the spin chain, we take into account the nearest-neighbor exchange, the single-ion anisotropy, and the dipolar interaction, writing

$$\mathscr{H} = -\frac{JS^2}{2}\sum_i \boldsymbol{\mu}_i \cdot \boldsymbol{\mu}_{i+1} - \frac{g\mu_{\rm B}S}{2}\sum_i \boldsymbol{\mu}_i \cdot \boldsymbol{H}_{\rm d} - \frac{\mathcal{K}S^2}{2}\sum_i \left(\boldsymbol{\mu}_i \cdot \boldsymbol{e}^i_{\rm T}\right)^2, \tag{2}$$

where J is the exchange integral, S is the length of the spin, $\boldsymbol{\mu}_i$ is the unit vector of the ith magnetic moment, $g = 2$ is the Landé factor, and $\mu_{\rm B}$ is the Bohr magneton. The dipolar field reads $\boldsymbol{H}_{\rm d} = -g\mu_{\rm B}S\sum_{j\neq i}[\boldsymbol{\mu}_j/r^3_{ij} - 3\boldsymbol{r}_{ij}(\boldsymbol{\mu}_j \cdot \boldsymbol{r}_{ij})/r^5_{ij}]$, with $\boldsymbol{r}_{ij}$ being the distance between the ith and jth magnetic moments. The last term in (2) represents the single-ion anisotropy with the coefficient $\mathcal{K}$ and anisotropy axis $\boldsymbol{e}^i_{\rm T} \equiv \boldsymbol{e}_{\rm T}(s_i)$, where s_i is the arc length for the ith spin. Here, the sums run over all N spins of the chain and the $(N+1)$-th spin corresponds to the first one. The distance between neighboring spins is a, which gives the curve length $L = (N+1)a$.

As the static σ models for ferro- and antiferromagnetic systems are presented by the same expressions, it is convenient to describe static macroscopic states of both systems, with ferromagnetic (FM) and antiferromagnetic (AFM) exchange coupling ($J > 0$ or $J < 0$, respectively), in terms of the vector order parameter $\boldsymbol{n}$. For FM systems, the physical meaning of $\boldsymbol{n}$ is the unit vector of magnetization, while for AFM systems, $\boldsymbol{n}$ represents the unit Néel vector. For the case of $J > 0$, the magnetic state of the chain is characterized by the unit vector of the order parameter $\boldsymbol{n}_i \equiv \boldsymbol{\mu}_i$, which is associated with the direction of the local magnetic moment of the chain. We refer to these samples as *FM epicycles*. We note that the temperature-dependent aspects of magnetism are beyond the focus of this study.

For the case of $J < 0$, we consider cases of even and odd values of N. For both of them, the primary order parameter $\boldsymbol{n}$ is the Néel vector (staggered magnetization), supplemented by the vector of ferromagnetism $\boldsymbol{m}$. In spin chains, these vectors can be introduced as $\boldsymbol{n}_i = (\boldsymbol{\mu}_{2i-1} - \boldsymbol{\mu}_{2i})/2$ and $\boldsymbol{m}_i = (\boldsymbol{\mu}_{2i-1} + \boldsymbol{\mu}_{2i})/2$, with $i = \overline{1, N/2}$. They obey the relations $\boldsymbol{n}_i \cdot \boldsymbol{m}_i = 0$ and $n_i^2 + m_i^2 = 1$ for each i. With this definition, $\boldsymbol{n}_i$ and $-\boldsymbol{n}_i$ represent the same physical state of the lattice, indicated by the double arrows in Fig. 1(a), where the magnetic sublattices are labeled by indices a, b. These samples are referred to as *AFM epicycles*. The same procedure can be carried out for the chains with odd N if the last magnetic moment, labeled as $\boldsymbol{\mu}_0$, is excluded from this dimerization procedure. These chains satisfy the criterion of a frustrated magnet by Toulouse

[46,47], having the negative total product of the exchange integrals. These samples are referred to as *frustrated epicycles*.

C. Representation of energy in the continuous limit

It is convenient to replace summation over the spin chain by integration over the continuous counterparts of the magnetic vectors, $\boldsymbol{n}_i \to \boldsymbol{n}(\boldsymbol{r})$, and, in the case of $J < 0$, also $\boldsymbol{m}_i \to \boldsymbol{m}(\boldsymbol{r})$. The anisotropy energy with the axis along $\boldsymbol{e}_\mathrm{T}$ reads $E_\mathrm{a}[\boldsymbol{n}] = -K \int n_\mathrm{T}^2 ds$. The anisotropy coefficient $K = K_\mathrm{a} + K_\mathrm{dip}$ consists of the contribution from the single-ion anisotropy $K_\mathrm{a} = \mathcal{K}S^2/(2a)$ [48] and dipolar interaction K_dip. The latter constant is characterized by the shape anisotropy and depends on the sign of the exchange integral, $K_\mathrm{dip}^\mathrm{fm} \approx 3.6(g\mu_\mathrm{B}S)^2/a^4$ for $J > 0$ (effective easy axis) and $K_\mathrm{dip}^\mathrm{afm} \approx -2.7(g\mu_\mathrm{B}S)^2/a^4$ for $J < 0$ (effective hard axis) [49].

The exchange energy for an AFM spin chain with even number of spins N reads [48]

$$E_\mathrm{x}[\boldsymbol{m}, \boldsymbol{n}] = \int [\Lambda m^2 + A_0(\partial_s \boldsymbol{n})^2 + \lambda \boldsymbol{m} \cdot (\partial_s \boldsymbol{n})]\, ds, \qquad (3)$$

with $\Lambda = 2|J|S^2/a$ being the constant of the uniform exchange which is responsible for the amplitude of magnetization m, $A_0 = |J|S^2 a$ the exchange stiffness, and $\lambda = 2|J|S^2$ the parity-breaking coefficient. If the magnetization is small, it can be excluded from the energy functional as a driving variable with the respective rescaling of the expression (3) as $E_\mathrm{x}[\boldsymbol{n}] = A \int \boldsymbol{n}'^2 ds$ with the exchange stiffness $A = A_0/2 = |J|S^2 a/2$. In this case, $\boldsymbol{m} = -0.5a\partial_s \boldsymbol{n}$. We note that for spin chains, the exchange stiffness is different in units by a^2 in comparison with the 3D simple cubic lattice in ferro- and antiferromagnets [50,51]. The same expression $E_\mathrm{x}[\boldsymbol{n}]$ is valid for FM chains. The closure of $\boldsymbol{\gamma}$ here can be taken into account via the periodic boundary conditions on the primary order parameter, $\boldsymbol{n}(0) \equiv \boldsymbol{n}(L)$ [48,52].

For the case of frustrated chains, the derivation procedure of the expression for exchange energy in the form (3) brings about two terms corresponding to the energy of a virtual defect associated with the unpaired moment $\boldsymbol{\mu}_0$; see Appendix B. In this case, the invariance of the expression (3) with respect to the freedom of choice of $\boldsymbol{\mu}_0$ in the chain introduces antiperiodic boundary conditions on the Néel vector, $\boldsymbol{n}(0) \equiv -\boldsymbol{n}(L)$. This is also in agreement with the theoretical [53] and experimental [54,55] investigation of AFM rings with odd number of spins, where the Möbius magnetic structure appears as a special case of the AFM spin spiral in a geometrically periodic system. In this way, an equilibrium magnetic texture of $\boldsymbol{n}$ for chains with both signs of J is determined by the variation of the total energy $E = E_\mathrm{x}[\boldsymbol{n}] + E_\mathrm{a}[\boldsymbol{n}]$, where the type of exchange bonds comes into the definition of the anisotropy only.

An interplay between the exchange and anisotropy energies allows one to introduce the effective magnetic length $\ell = \sqrt{A/|K|}$, which is a measure of spatial scales. In the following, the reduced coordinate $\xi = s/\ell$, chain length $X = L/\ell$, curvature $\varkappa = \kappa\ell$, and torsion $\sigma = \tau\ell$ are used. The aforementioned derivation of the continuum expressions for the magnetic energies is valid if $\ell \gg a$.

The exchange energy density in a curvilinear reference frame can be split into three terms, $E_\mathrm{x}[\boldsymbol{n}] = |K|\ell \int (w_\mathrm{x}^0 + w_\mathrm{x}^\mathrm{D} + w_\mathrm{x}^\mathrm{an}) d\xi$, where $w_\mathrm{x}^0 = (n'_\alpha)(n'_\alpha)$ is the locally homogeneous part of exchange and prime means the derivative with respect to ξ, $w_\mathrm{x}^\mathrm{D} = \epsilon_{\alpha\beta\gamma} d_\alpha n_\beta n'_\gamma$ is the curvature-induced DMI, and $w_\mathrm{x}^\mathrm{an} = \mathcal{F}_{\alpha\gamma}\mathcal{F}_{\beta\gamma} n_\alpha n_\beta$ is the curvature-induced anisotropy [49]. Here, the Einstein summation rule is used, Greek indices run over the local reference frame, $\alpha, \beta, \gamma = \overline{\mathrm{T}, \mathrm{N}, \mathrm{B}}$, $\epsilon_{\alpha\beta\gamma}$ is the totally antisymmetric Levi-Civita symbol, $\boldsymbol{d} = 2\sigma \boldsymbol{e}_\mathrm{T} + 2\varkappa \boldsymbol{e}_\mathrm{B}$ is the Dzyaloshinskii vector, and $\mathcal{F}_{\alpha\beta}$ is the Frenet tensor with nonzero components $\mathcal{F}_\mathrm{TN} = -\mathcal{F}_\mathrm{TN} = \varkappa$ and $\mathcal{F}_\mathrm{NB} = -\mathcal{F}_\mathrm{BN} = \sigma$. The latter allows one to define $w_\mathrm{x}^\mathrm{an} = k_{11} n_\mathrm{T}^2 + k_{22} n_\mathrm{N}^2 + k_{33} n_\mathrm{B}^2 - k_{13} n_\mathrm{T} n_\mathrm{B}$ with $k_{11}(\xi) = \varkappa^2$, $k_{33} = \sigma^2$, $k_{22} = k_{11} + k_{33}$, and $k_{13}(\xi) = 2\varkappa\sigma$. The anisotropy w_x^an is the source of the easy-axis anisotropy lying in the rectifying (TB) plane, in addition to the hard-axis anisotropy E_a stemming from the dipolar interaction. A nonzero $\boldsymbol{d}$ can result in spin spiral states [49]. The distribution of $\boldsymbol{d}$ along the epicycle $\boldsymbol{\gamma}_{-3}^1$ is shown in Fig. 1(f). Because of the selection of the geometry, only the binormal component of $\boldsymbol{d}$ is coordinate dependent. The strongest curvature-induced DMI appears at the knots, where $\boldsymbol{d}$ is almost aligned with the binormal direction, while in the remaining part of the closed curved, it follows the tangential direction.

IV. MAGNETIC STATES

A static state within the nonlinear σ model described in Sec. III C is not sensitive to the sign of J. Still, it strongly depends on the (anti)periodicity of the boundary conditions. Therefore, first we consider the two cases of the easy- and hard-axis anisotropy in FM and AFM epicycles and then analyze the frustrated epicycles with both cases of the anisotropy coefficient K. In this section, we focus on the case of small torsion, $|\sigma| \ll 1$, which corresponds to values of $\mathscr{R}$ large enough for anisotropic effects to dominate over exchange ones. For large torsions, spin chains can experience the helimagnetic phase transition [17,49], which is discussed in Appendix D.

A. FM and AFM epicycles with the easy-axis anisotropy

In this section, we focus on the FM and AFM epicycles γ_p^1 with the easy-axis anisotropy ($K > 0$). We start from the case of a magnetically hard system, with the contribution of anisotropy being much stronger than the dipolar interaction, i.e., $K_\mathrm{a} \gg K_\mathrm{dip}$. It is convenient to introduce the local spherical parametrization of the order parameter as

$$\boldsymbol{n} = \sin\Theta_\mathrm{ea}(\cos\Phi_\mathrm{ea}\boldsymbol{e}_\mathrm{T} + \sin\Phi_\mathrm{ea}\boldsymbol{e}_\mathrm{N}) + \cos\Theta_\mathrm{ea}\boldsymbol{e}_\mathrm{B}, \qquad (4)$$

with $\Theta_\mathrm{ea}(\xi)$ and $\Phi_\mathrm{ea}(\xi)$ being magnetic polar and azimuthal angles following the periodic boundary conditions. Here and in the following, the magnetic polar angles are defined within the $[0, \pi]$ range and the magnetic azimuthal angles can take arbitrary values. For $|\sigma| \ll 1$, the ground state reads $\Theta_\mathrm{ea} = \pi/2 + \vartheta_\mathrm{ea}(\xi)$ and $\Phi_\mathrm{ea} = 0.5(1 \mp 1)\pi + \varphi_\mathrm{ea}(\xi)$, where $\vartheta_\mathrm{ea}, \varphi_\mathrm{ea} \ll 1$ satisfy equations of the nonlinear pendulum with an external drive and parametric pumping,

$$\vartheta''_\mathrm{ea} - [1 + k_{11}(\xi)]\vartheta_\mathrm{ea} = \pm k_{13}(\xi) \equiv \pm\sigma\varkappa(\xi), \qquad (5a)$$

$$\varphi''_\mathrm{ea} - \varphi_\mathrm{ea} = -\frac{d'_\mathrm{B}(\xi)}{2} \equiv -\varkappa'(\xi). \qquad (5b)$$

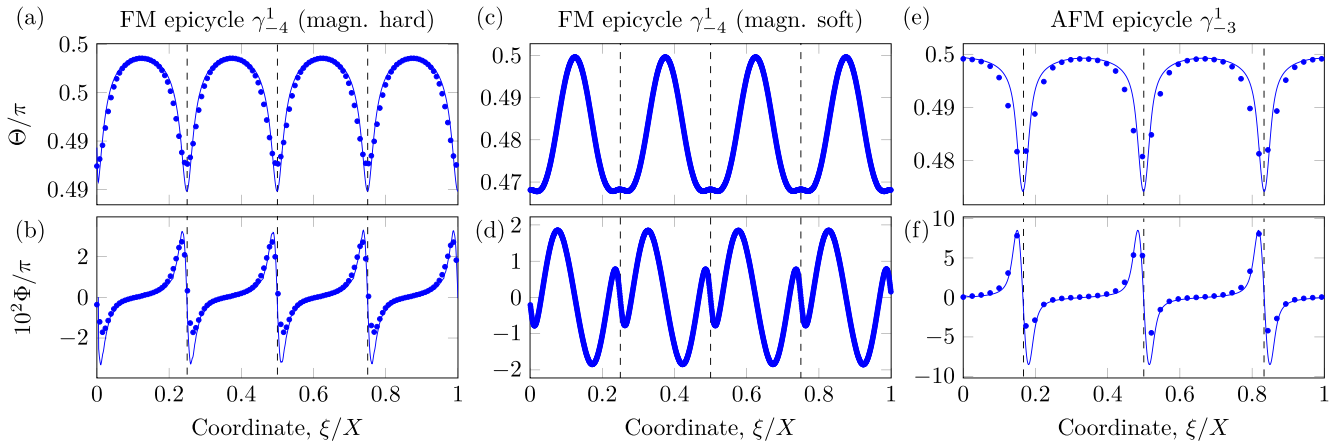

FIG. 2. Ground states of FM and AFM epicycles with the easy-axis anisotropy and $\sigma = 0.1$ (quasitangential state). (a) Polar and (b) azimuthal angles of the order parameter $\boldsymbol{n}$ in a magnetically hard ($K_{\rm dip} \ll K_{\rm a}$) FM epicycle γ^1_{-4}. Symbols and solid lines correspond to simulations and Eq. (6), respectively. [(c),(d)] The same for a magnetically soft FM epicycle γ^1_{-4} ($K_{\rm a} = 0$). Only simulation results are shown. The magnetic state is perturbed by the long-range part of the dipolar interaction. [(e),(f)] The same for an AFM epicycle γ^1_{-3} with the dominating single-ion anisotropy. In panels (a), (b), (e), and (f), each 10th symbol in the simulations is shown. In all panels, the black dashed lines show positions, where the curvature is maximal.

These angles also satisfy the periodic boundary conditions $\vartheta_{\rm ea}(0) = \vartheta_{\rm ea}(X)$ and $\varphi_{\rm ea}(0) = \varphi_{\rm ea}(X)$. By neglecting parametric pumping determined by $k_{11}(\xi)$ in Eq. (5a), which also implies that $\varkappa(\xi) \ll 1$, the system (5) can be solved asymptotically. The respective polar and azimuthal angles of the order parameter read

$$\Theta_{\rm ea}(\xi) = \frac{\pi}{2} \mp \sigma\varkappa(\xi) + \mathcal{O}(\varkappa^2),$$
$$\Phi_{\rm ea}(\xi) = \frac{1 \mp 1}{2}\pi + \varkappa'(\xi) + \mathcal{O}\left(\frac{|\varkappa'''|}{|\varkappa'|}\right). \tag{6}$$

We refer to this state as the quasitangential state. Naturally, the main deviation from the purely tangential state occurs in the vicinity of the knots of the epicycle, corresponding to the maximum of curvature. The comparison of the solution (6) with simulations is shown in Fig. 2. As it follows from numerical analysis, the solution (6) matches the simulation data with a good accuracy, even for $\varkappa(\xi) \lesssim 1$. For both FM and AFM epicycles with $\sigma = 0.1$ [Figs. 2(a), 2(b), 2(e), and 2(f)], there is a small difference between the analytics and simulations near the maxima of the curvature, where $\varkappa_{\max} \approx 0.48$ for the FM epicycle γ^1_{-4} and $\varkappa_{\max} \approx 1$ for the AFM epicycle γ^1_{-3}. While the net magnetization of the AFM epicycle is zero, the FM epicycles develop a small moment along the symmetry axis of the geometry. For the γ^1_{-4} sample with $\sigma = 0.1$, the net moment is about 1% of the saturation value.

The ground state of the magnetically soft epicycle ($K_{\rm a} = 0$) is also close to the tangential state, although the magnetic state cannot be described by Eqs. (6); see Figs. 2(c) and 2(d). Unlike the aforementioned case of hard magnetic material, both spherical angles deviate from the tangential direction in a spread region around the maxima of curvature. In particular, the spatial distribution of the azimuthal angle has wave vectors corresponding to the wavelengths $X/|p|$ and $2X/|p|$. This behavior originates from the long-range part of the dipolar interaction, which leads to the self-interaction of the neighboring parts of the epicycle similarly to the experimental observations in planar [56] and 3D ferromagnetic geometries [57]. We note that the quasitangential ground state is an analogy of the vortex state in planar rings with easy-axis anisotropy [58].

B. FM and AFM epicycles with the hard-axis anisotropy

In this section, we focus on the FM and AFM epicycles γ^1_p with the hard-axis anisotropy ($K < 0$). In comparison with the easy-axis magnets (Sec. IV A), a possibility to pin an inhomogeneous magnetic texture at the epicycle knots supports a variety of metastable states and complicates the determination of the ground state. Therefore, in the following, we describe the lowest-energy states that are numerically found. The discussion of a possibility to have these states as the ground state is given in Sec. VI.

A convenient angular parametrization for the order parameter in the system with the hard tangential axis of anisotropy is

$$\boldsymbol{n} = \cos\Theta_{\rm ha}\boldsymbol{e}_{\rm T} + \sin\Theta_{\rm ha}(\cos\Phi_{\rm ha}\boldsymbol{e}_{\rm N} + \sin\Phi_{\rm ha}\boldsymbol{e}_{\rm B}), \tag{7}$$

with the polar and azimuthal angles $\Theta_{\rm ha}$ and $\Phi_{\rm ha}$, respectively, which follow the periodic boundary conditions. As it is known for AFM rings with the even number of spins and AFM helices [49], their ground state is close to the binormal one with $\Theta_{\rm ha} = \Phi_{\rm ha} = \pi/2$. This happens due to the appearance of a weak easy-axis anisotropy of the exchange origin with the coefficient $k_{11}(\xi)$. The corresponding static state on the background of the binormal state, $\Theta_{\rm ha} = \pi/2 + \vartheta_{\rm ha}(\xi)$ and $\Phi_{\rm ha} = \pm\pi/2 + \varphi_{\rm ha}(\xi)$, where $\vartheta_{\rm ha}, \varphi_{\rm ha} \ll 1$, satisfies the equations

$$\vartheta''_{\rm ha} - [1 + k_{11}(\xi)]\vartheta_{\rm ha} = \pm\left(k_{13}(\xi) - \frac{d'_{\rm B}(\xi)}{2} + \frac{d_{\rm B}(\xi)\varphi'_{\rm ha}}{2}\right), \tag{8a}$$

$$\varphi''_{\rm ha} - k_{11}(\xi)\varphi_{\rm ha} = \mp\frac{[\vartheta_{\rm ha}d_{\rm B}(\xi)]'}{2}, \tag{8b}$$

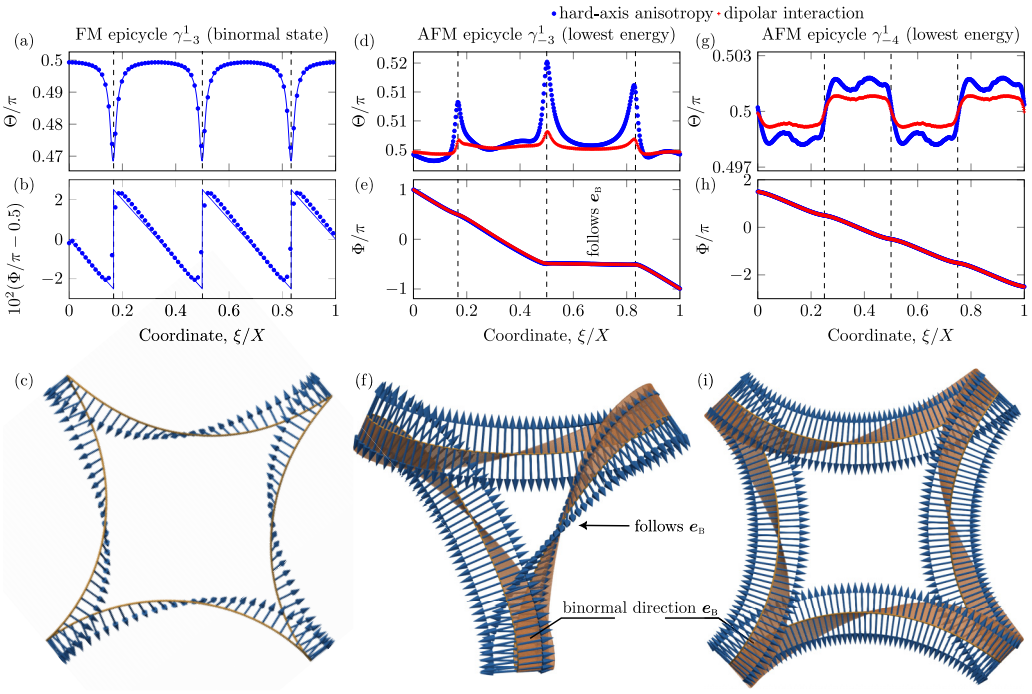

FIG. 3. Magnetic states of FM and AFM epicycles with the hard-axis anisotropy and $\sigma = 0.1$. (a) Polar and (b) azimuthal angles of the order parameter $\boldsymbol{n}$ in the FM epicycle γ^1_{-3}. Symbols (each 10th simulated data point is shown) and solid lines correspond to simulations and Eq. (9), respectively. The black dashed lines show positions, where the curvature is maximal. (c) The quasibinormal magnetic state of the FM epicycle γ^1_{-4} in simulations; cf. Fig. 1(f). The blue arrows correspond to the direction of each third local magnetic moment. (d)–(f) and (g)–(i) show the same for the 2π-twist and 4π-twist states (lowest-energy states) of the AFM epicycles γ^1_{-3} [cf. Fig. 1(a)] and γ^1_{-4}. The blue symbols and red crosses correspond to the cases of the hard-axis anisotropy and dipolar interaction, respectively. In (f) and (i), the blue arrows show equidistant magnetic moments from the opposite sublattices (each third site is shown). A semitransparent yellow surface indicates the direction of $\boldsymbol{e}_B$, which coincides with the magnetic moment's axes only within certain segments of the epicycle indicated in (f).

with the periodic boundary conditions $\vartheta_{ha}(0) = \vartheta_{ha}(X)$ and $\varphi_{ha}(0) = \varphi_{ha}(X)$. Similarly to the case of FM epicycles, the polar angle in the binormal state can be found asymptotically. The azimuthal angle is a solution of the equation with strongly nonlinear coefficients and can be approximated by a linear function. Together they read

$$\Theta_{ha}(\xi) = \frac{\pi}{2} \mp \sigma\varkappa(\xi) + \mathcal{O}(\varkappa^2),$$
$$\Phi_{ha}(\xi) \approx \pm\frac{\pi}{2} + \frac{\sigma}{2}\left[\frac{\pi}{2} - \left(p\pi\frac{\xi}{X} - \frac{\pi}{2}\right)\mathrm{mod}\,\pi\right]. \quad (9)$$

This expression fits the spatial distribution of the order parameter for FM and AFM epicycles; see Figs. 3(a)–3(c). We refer to the state (9) as the quasibinormal state.

Surprisingly, the state (9) is not the ground state for these epicycles. The lowest-energy state of the epicycle γ^1_{-3} consists of two spatial regions with different behavior of the order parameter [Figs. 3(e) and 3(f)]. There is a segment of the epicycle in which the order parameter follows the binormal direction, which looks as a twist drawn by $\boldsymbol{n}$ in space [Figs. 1(a) and 3(f)]. In the remaining part of the geometry, the order parameter slowly rotates by π radians around $\boldsymbol{e}_T$ on each of the segments, which looks like the almost uniform distribution of $\boldsymbol{n}$ in the laboratory reference frame (2π-twist state).

The AFM epicycle γ^1_{-4} [Figs. 3(g)–3(i)] in the lowest-energy state has a π twist of the order parameter $\boldsymbol{n}$ within each of its segments. The respective 4π-twist state is shown in Figs. 3(g)–3(i). This geometry also supports 2π-twist states with two segments following the quasibinormal state. Among 2π-twist states, the most symmetric case with quasibinormal distribution at the oppositely placed segments has the lowest energy. If the quasibinormal distribution is obtained in two sequential states, the energy is slightly larger because of the modification of the magnetic texture at the knots.

We stress that the discussed states of the epicycles with easy and hard axis of anisotropy are the same in terms of the order parameter $\boldsymbol{n}$ for both FM and AFM cases considered in these sections. For all of them, the excited states include domain walls pinned at the epicycle knots. While the hard-axis AFM epicycles are magnetically compensated as the easy-axis ones, the FM epicycles develop a strong magnetic moment in plane perpendicular to the symmetry axis of the order of the saturation value. It is supplemented by a small magnetic moment along the symmetry axis.

In the case of the absence of the single-ion anisotropy in spin chains with the AFM exchange bonds, the dipolar interaction leads to an effective hard-axis anisotropy. We found that in this case, the azimuthal angle Φ agrees well with the results of the simulations with the hard-axis anisotropy only [Figs. 3(d), 3(e), 3(g), and 3(h), red crosses]. The difference is in the amplitude of the change of the polar angle Θ, which is smaller for the case of dipolar interaction. The simulations are done for the nominally same magnetic lengths in both cases. Thus, we expect that the origin of the difference between $\Theta(\xi)$ in these simulations arises due to the partial uncompensation of the antiferromagnetically ordered

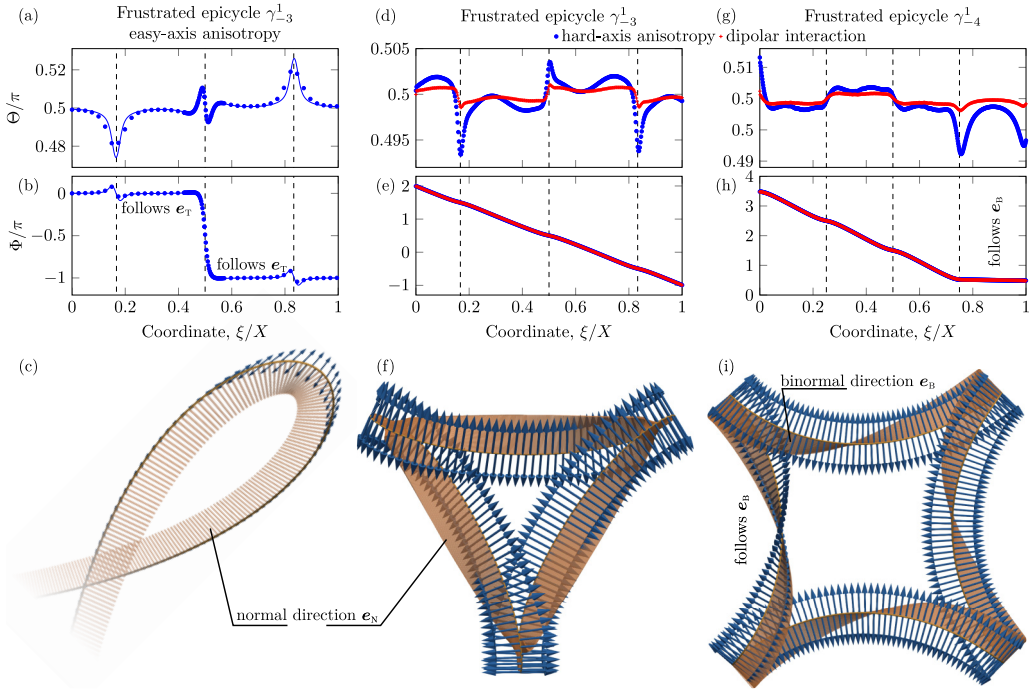

FIG. 4. Ground states of frustrated epicycles with the easy-axis anisotropy and $\sigma = 0.1$. (a) Polar and (b) azimuthal angles of the order parameter $\boldsymbol{n}$ in a frustrated epicycle γ^1_{-3} with the easy-axis anisotropy. Symbols and solid lines (drawn outside the domain-wall region) correspond to simulations and Eq. (6), respectively. Outside the domain wall, each 10th simulated data port is shown. (c) Zoom of the knot hosting the domain wall in simulations. Blue arrows show individual magnetic moments. Yellow cylinders indicate the normal direction $\boldsymbol{e}_N$. (d)–(f) and (g)–(i) are the same for the frustrated epicycles γ^1_{-3} and γ^1_{-4} with the hard-axis anisotropy (blue symbols) and dipolar interaction (red crosses), respectively (3π-twist state). In (f) and (g), a semitransparent yellow surface indicates the direction of $\boldsymbol{e}_N$ and $\boldsymbol{e}_B$, respectively. Each third magnetic moment is shown.

spins near the epicycle knots, similarly to FM epicycles [cf. Fig. 2(d)].

C. Magnetic states in frustrated epicycles

In this section, we consider epicycles with the AFM nearest-neighbor exchange and odd number of spins. Their magnetic states follow the same equations for the angular variables introduced in (4) and (7) for the easy- and hard-axis anisotropies, respectively. The difference is that here the antiperiodic boundary conditions are applied for $\boldsymbol{n}$, i.e., $\Theta_{\text{ea,ha}}(0) = \pi - \Theta_{\text{ea,ha}}(X)$ and $\Phi_{\text{ea,ha}}(0) = \Phi_{\text{ea,ha}}(X) + \pi + 2\pi w$ with $w \in \mathbb{Z}$. For the case of planar rings, the ground state corresponds to the so-called Möbius state with the order parameter making one twist around the circle [53].

For frustrated epicycles with the easy-axis anisotropy, the antiperiodic boundary conditions impose the appearance of a domain wall in the ground state. The domain wall is located at one of the knots because of the strong curvature-induced DMI at this location. Far from the domain wall, the magnetic state can be approximately described by Eqs. (6); see Figs. 4(a)–4(c).

Hard-axis frustrated epicycles with even and odd number of knots have different lowest-energy states. In the lowest-energy state, the magnetic texture of each of three segments of the γ^1_{-3} epicycle is almost uniform in the laboratory reference frame, which corresponds to the rotation of $\boldsymbol{n}$ by π radians around the tangential direction (3π-twist state) [Figs. 4(d)–4(f)]. The epicycle with four knots in the lowest-energy state has 3π twist over three segments, and one segment in the quasibinormal state [Figs. 4(g)–4(i)]. We note that in case of the change of the hard-axis anisotropy to the dipolar interaction in simulations, the observed changes in the magnetic state are the same as for AFM epicycles; cf. Figs. 3(d), 3(e), 3(g), and 3(h), and Figs. 4(d), 4(e), 4(g), and 4(h). The frustrated epicycles develop zero net magnetization in the ground state.

V. FERROTOROIDAL ORDERING

The closed-loop spin chains that are studied here lack both space-inversion and time-reversal symmetries. This makes them a potential host for magnetoelectric multipoles defined by [9] $\mathcal{M}_{ij} = \int \mathbf{r}_i \boldsymbol{\mu}_j(\mathbf{r}) d^3\mathbf{r}$ that can be decomposed into three irreducible tensors: the pseudoscalar $A = \text{tr}\mathcal{M}_{ij}/3$ defining the magnetoelectric monopole [59], the toroidal moment related to the antisymmetric part $\mathbf{T} = \epsilon_{ijk}\mathcal{M}_{jk}/2$, and the traceless symmetric tensor describing the quadrupole magnetic moment. These three components of the $\mathcal{M}_{ij}$ tensor are of paramount importance to the linear magnetoelectric response $\|\alpha_{ij}\|$, $i, j = x, y, z$. Before computing the magnetoelectric multipoles in our closed-loop spin chains, we recall that one of the main complications in their definition is their origin dependence for uncompensated magnetic textures. In the following, we will take into account only the contribution from the *compensated* part of the spin texture that is instead origin independent.

First, we use a Landau field theory that incorporates ferroelectric polarization $\boldsymbol{P}$ and magnetization $\boldsymbol{M}$. Since the

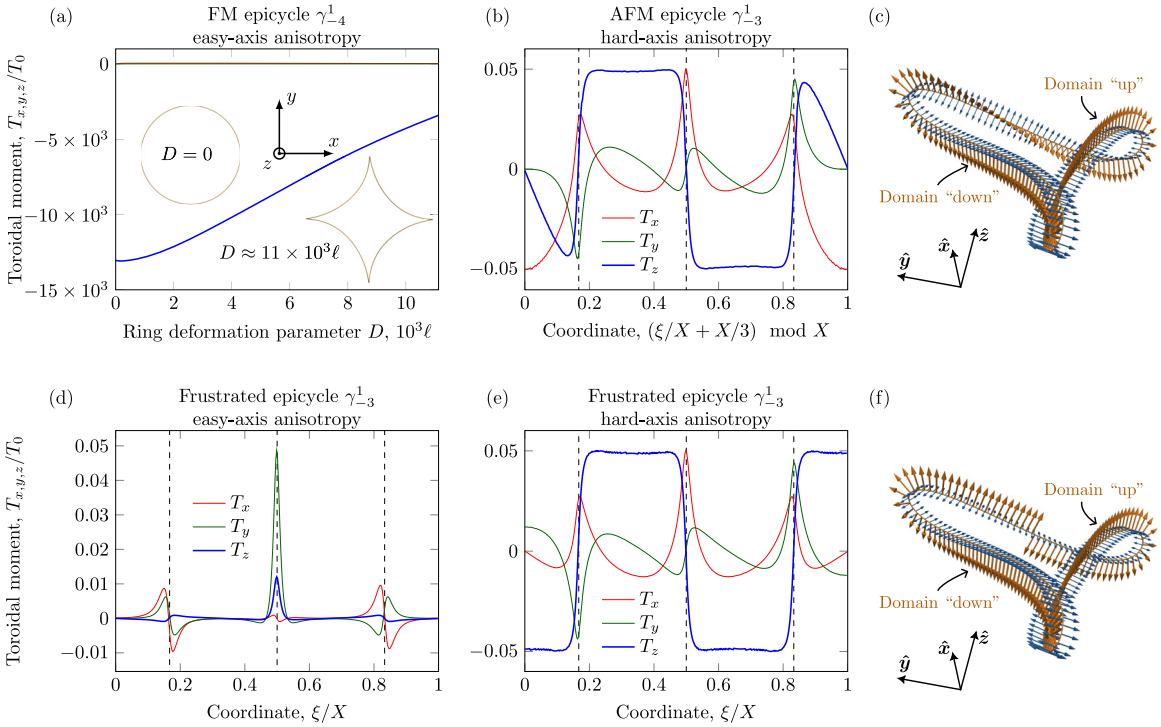

FIG. 5. Ferrotoroidal ordering in magnetic epicycles. (a) The total toroidal moment of a ferromagnetic spin chain deformed from a ring ($D = 0$) to the epicycle γ^1_{-4} [$D \approx 11 \times 10^3$, the same as the one shown in Figs. 2(a) and 2(b)]. Insets show the axial views of the respective geometries. The coordinate system (x, y, z) is shown as well. (b) Local toroidal moment in the AFM epicycle γ^1_{-3} with the hard-axis anisotropy and (c) its 3D view with the blue and orange arrows showing the magnetic and toroidal moments, respectively (each third site is shown). The corresponding state is shown in Figs. 3(d)–3(f); note the shift by $X/3$ in the coordinate. (d) The same for a frustrated epicycle γ^1_{-3} with the easy-axis anisotropy. The corresponding state is shown in Figs. 4(a)–4(c). [(e),(f)] The same for a frustrated epicycle γ^1_{-3} with the hard-axis anisotropy. The corresponding state is shown in Figs. 4(d)–4(f).

epicycles γ^1_{-3} and γ^1_{-4} are characterized by the presence of 3_z or 4_z axes of rotation, respectively, the free-energy terms for the variable $\boldsymbol{O}$ with $\boldsymbol{O} = \boldsymbol{M}$ or $\boldsymbol{P}$ are the same. In particular, the free energy allows terms O^2 and O_z^2 of the second order, and terms M^4, P^4, M^2P^2, $(\boldsymbol{M} \cdot \boldsymbol{P})^2$ of the fourth order. The magnetoelectric coupling term reads

$$F_{\mathrm{ME}} = \alpha_{xx}(M_xP_x + M_yP_y) + \alpha_{zz}M_zP_z + \alpha_{xy}(M_xP_y - M_yP_x), \tag{10}$$

with the $\hat{\boldsymbol{z}}$ axis along the symmetry axis of the structure. The first two terms in Eq. (10), as the diagonal part of the magnetoelectric coupling, can be decomposed in the magnetoelectric monopolization a and the q_{x^2}, q_{y^2}, and q_{z^2} components of the quadrupolar moment with the additional constraint $q_{x^2} \equiv q_{y^2}$ and the traceless condition $q_{x^2} + q_{y^2} + q_{z^2} \equiv 0$. The last term instead indicates the magnetoelectric coupling corresponding to the toroidal moment $\boldsymbol{T}$ directed along $\hat{\boldsymbol{z}}$. The other components of the toroidal moment as well as the quadrupolar moment components q_{ij} with $i \neq j$ are not allowed by symmetry.

We proceed with the calculation of the change in the total toroidal moment in a FM system for the smooth change of the geometry of the epicycle into a ring; see Fig. 5(a). The geometry transformation is calculated by mimicking the mechanical forces acting in the plane perpendicular to the epicycle's axis. To describe these changes, we characterize each geometry by the deformation parameter $D = \sum_{i=0}^{N-1} |\boldsymbol{r}_i - \boldsymbol{r}_i^{\mathrm{circ}}|$, where $\boldsymbol{r}_i^{\mathrm{circ}}$ is the radius vector of the ith spin at the ring. In this way, the quasitangential state (6) is smoothly translated into a vortex state on the ring [58]. Selecting the origin for the radius vector of the ith moment $\boldsymbol{r}_i$ in the center of mass of the sample, we obtain the origin-independent value of the toroidal moment by accounting for the compensated part of the magnetization only. Figure 5(a) shows that $T_z(D)$ smoothly changes with the geometry transformation, in agreement with the symmetry of the free energy (10). The numerical values of the in-plane components of the toroidal moment, as well as of the monopole moment and components of the quadrupole moments, are of the same order and about 200 times smaller than T_z. We correlate their finite values with the discrete structure of the spin chain.

The fact that only the z component of the toroidal moment is nonvanishing implies that the spin texture realizes a purely toroidal configuration, similarly to Bloch skyrmions [60]. We note that for a vortex state on a ring, this purely toroidal state is symmetry enforced. The vertical mirror symmetries imply that the magnetoelectric monopole, as well as the quadrupole moment components q_{x^2,y^2,z^2}, must vanish. In addition, the $T_{x,y}$ components are zero due to the planar spin configuration. In the epicycles, instead, these symmetries are not present. Therefore, the purely toroidal configuration is spontaneously chosen by the spin texture. We note that the case of a hard-axis FM epicycle is more complex and the corresponding magnetic

state can support finite monopole or quadrupolar contributions in addition to the toroidal moment.

In the following, we discuss magnetoelectric monopoles in AFM and frustrated epicycles. As magnetic monopoles of the two magnetic "sublattices" are equal and opposite, the *total* value of the magnetoelectric monopoles is negligibly small. Still, the *local* values of the magnetoelectric monopoles from each pair of magnetic moments can be different from zero. For instance, the local value of $\boldsymbol{T}(\xi)$ can be calculated for each pair $\boldsymbol{\mu}_{2i-1,2i}$ on which $\boldsymbol{n}_i$ is introduced with respect to its center,

$$\boldsymbol{t}_i = \frac{1}{2\ell}\left[\left(\boldsymbol{r}_{2i-1} - \boldsymbol{r}_i^c\right) \times \boldsymbol{\mu}_{2i-1} + \left(\boldsymbol{r}_{2i} - \boldsymbol{r}_i^c\right) \times \boldsymbol{\mu}_{2i}\right] - \frac{1}{2\ell}\boldsymbol{r}_i^c \times (\boldsymbol{\mu}_{2i-1} + \boldsymbol{\mu}_{2i}), \tag{11}$$

with $\boldsymbol{r}_i^c = 0.5(\boldsymbol{r}_{2i-1} + \boldsymbol{r}_{2i})$. AFM epicycles with the odd number of knots show the presence of well-defined toroidal domains in the laboratory reference frame oriented along the axis of symmetry located between the epicycle's knots; see the blue line in Figs. 5(b) and 5(c) for the epicycle γ_{-3}^1. Here, the opposite toroidal domains correspond to the almost linearly changing Φ in Fig. 3(e). The same picture with three sequential toroidal domains is observed for the frustrated epicycle γ_{-4}^1.

An easy-axis frustrated epicycle shows a pronounced change of $\boldsymbol{T}$ only at knots with the maximum value reached at the domain wall [Fig. 5(d)]. This finding is in agreement with the expectation of the finite magnetization at the inhomogeneous distribution of the Néel vector in spin chains [48]. The symmetry of $\boldsymbol{T}(\xi)$ in a hard-axis frustrated epicycle γ_{-3}^1 [Figs. 5(e) and 5(f)] is different from the AFM epicycle with three knots [Fig. 5(b)] due to antiperiodic boundary conditions. These distinct features are expected to affect the local ferroelectric polarization that can be induced by externally applying a magnetic field via the trilinear coupling $\boldsymbol{T} \times \boldsymbol{P} \cdot \boldsymbol{M}$. For instance, for AFM epicycles with three knots, we expect ferroelectric domains with equal and opposite polarization along the $\hat{\boldsymbol{x}}$ direction if a constant magnetic field along the $\hat{\boldsymbol{y}}$ direction is applied. We note that a finite net toroidal moment T_x for the frustrated epicycle with hard-axis anisotropy [Fig. 5(e)] can lead to a finite magnetic moment along the $\hat{\boldsymbol{z}}$ ($\hat{\boldsymbol{y}}$) direction in the presence of a finite electric field along the $\hat{\boldsymbol{y}}$ ($\hat{\boldsymbol{z}}$) direction.

VI. COMPARISON OF MAGNETIC TEXTURES IN EPICYCLES

Here, we described static magnetic states in curvilinear closed spin chains with constant torsion σ. We focused on cases of the easy- and hard-axis anisotropies in spin chains with FM nearest-neighbor exchange as well as chains with AFM exchange containing odd or even number of spins. The particular case of space curves with constant torsion discussed in this work complements the results known for planar rings and helices, both with $\varkappa = \text{const}$ and $\sigma = \text{const}$. The case of closed curves allows us to focus on the geometries topologically related to planar rings and track the change of their magnetic textures with the change of geometry. Nevertheless, unlike planar rings, the Dzyaloshinskii vector $\boldsymbol{d}$ in curves of constant torsion always has a nonvanishing tangential component, which may compete with other curvature-induced and intrinsic interactions.

For easy-axis FM and AFM epicycles, the ground state is the quasitangential state with the order parameter $\boldsymbol{n}$ directed almost along the tangential direction with a small deviation near the knots; see Fig. 2. The effects of a finite torsion are pronounced in hard-axis samples, where the geometry-driven Dzyaloshinskii vector $\boldsymbol{d}$ is almost perpendicular to the order parameter $\boldsymbol{n}$ on a major part of the spin chain. Hence, it can lead to spin spiral and topologically nontrivial states when taking into account the boundary conditions for $\boldsymbol{n}$ in closed chains. The lowest-energy state for hard-axis AFM epicycles with even number of spins and FM epicycles is more complex (Fig. 3) and can be understood by comparing with frustrated epicycles which have AFM exchange and odd number of spins (Fig. 4). The local state in each geometric segment of the epicycle is determined by the following aspects: (i) The condition of a constant torsion σ implies a constant tangential component of the curvature-induced Dzyaloshinskii vector $\boldsymbol{d}$. (ii) The curvature changes in a wide range of values from $\varkappa \ll \sigma$ at the center of the segment to $\varkappa \gtrsim \sigma$ at its ends; see Fig. 1(b). Thus, unlike the geometry-driven anisotropy, the geometry-driven DMI is never vanishing and can lead to a spin spiral state.

The local ground state for the case of constant or very slowly varying σ and $\varkappa$ is determined by their balance: for $\sigma \lesssim \varkappa$, the state in the local reference frame is uniform (twisted in the laboratory reference frame). Otherwise, the spin chain is in a helicoidal state, which is almost uniform in the laboratory reference frame [49]. Thus, in the central part of the epicycle's segment, the curvature-induced DMI dominates over the curvature-induced anisotropy, thus favoring rotations of $\boldsymbol{n}$ around $\boldsymbol{d} \approx \boldsymbol{e}_\text{T}$. At the segment's ends, the physical picture is opposite: the curvature-induced anisotropy w_x^an determined by $\varkappa$ cannot be considered to be small and induces an easy axis along $\boldsymbol{e}_\text{B}$. Together with a strong curvature-induced DMI $\boldsymbol{d} \approx 2\varkappa\boldsymbol{e}_\text{B}$, the curvature-induced anisotropy produces a pinning potential for inhomogeneous magnetic textures.

Therefore, the segments can support the following magnetic states: (i) binormal state if the energy contribution from knots dominates, (ii) helicoidal state if the energy contribution from the central part dominates, and (iii) mixed state resembling features of the binomial and helicoidal states. Although the size of the epicycle's segment and the helicoid period is $\sim 1/\sigma$, the only possible rotation of $\boldsymbol{n}$ corresponding to the minimal energy corresponds to the twist by π radians. The total change of the magnetic azimuthal angle Φ over the whole geometry in AFM and FM epicycles should be a multiple of 2π to match the periodic boundary conditions. The segments accommodating the change of Φ by π are almost magnetically uniform in the laboratory reference frame [top and left segments of the γ_{-3}^1 epicycle in Fig. 3(f), and all segments of the γ_{-4}^1 epicycle in Fig. 3(i)]. The energy contribution from knots is important for small-size epicycles (large σ, which leads to a much larger $\varkappa_\text{max}$); see Appendix D. In this case, the lowest-energy state corresponds to an almost uniform texture in the laboratory reference frame with $\boldsymbol{n}$ directed along the axis of symmetry. We note that this state corresponds to a helicoidal state in the local reference frame.

Frustrated epicycles maintain the total phase equal $(2w+1)\pi$ with $w \in \mathbb{N}$, which allows the texture to fit the antiperiodic boundary conditions. Since the π-twist state (with two segments being in a quasibinormal state) of a frustrated epicycle γ^1_{-3} has higher energy than the 3π-twist state for the geometries under consideration, the helicoidal texture within the segment is energetically more preferable than the binormal state. This is an indication that the influence of the curvature-driven DMI dominates over the anisotropy in the magnetic energy. Based on the symmetry considerations, the described lowest-energy states for FM and AFM epicycles can be considered as the ground states for the geometries γ^1_{-3} and γ^1_{-4}. This conclusion can be extrapolated to epicycles with $|p| > 4$ if their segment length is much larger than ℓ.

For easy-axis systems, only the case of magnetically soft FM epicycles is special because of the self-interaction between the epicycle's segments via the dipolar interaction. The hard-axis systems reveal more specific geometry-dependent behavior. Here, there are two origins of the geometric frustration. The first one is the odd number of spins relevant for AFM-coupled spin chains [Figs. 4(d)–4(i)], which enforces the antiperiodic boundary condition for $\boldsymbol{n}$. The second origin of frustration is introduced by the epicycle knots separating regions, which may have different magnetic textures. In this case, it is possible to track how the specific magnetic states can emerge either due to the even (odd) number of spins or due to the odd (even) number of knots in the epicycle. In particular, the 2π state, which contains a segment in a quasibinormal state, in an AFM epicycle with the odd number of knots γ^1_{-3} [Figs. 3(d)–3(f)] resembles a frustrated epicycle with the even number of knots γ^1_{-4} [Figs. 4(g)–4(i)], and vice versa [cf. Figs. 3(g)–3(i) and 4(d)–4(f)]. As a rule of thumb, the state of a hard-axis spin chain is magnetically frustrated if the sum of the knots and spins $Q = (|p| + N) \mod 2$ is nonzero.

A specific feature of the geometries with (anti)periodic boundary conditions is the possibility to develop a finite toroidal moment $\boldsymbol{T}$, which provides a bridge between the magnetic and electric degrees of freedom [38]. In this respect, easy-axis ferromagnetic spin chains can be characterized by a macrotoroidal moment depending on their shape [Fig. 5(a)]. Hard-axis epicycles split into a multidomain state by $\boldsymbol{T}$ with a sizable axial component T_z. The aforementioned interplay between the frustration of the magnetic state produced either by the odd number of spins or the odd number of knots is also reflected in the formation of toroidal domains: a series of oppositely oriented domains appears for $Q = 1$.

VII. CONCLUSIONS AND OUTLOOK

To summarize, the presented analysis shows that the geometric frustration in magnetic systems can appear due to specific distributions of the curvature and torsion in a spin chain because of spatial distribution of the geometry-driven Dzyaloshinskii-Moriya interaction and interplay with the (anti)periodic boundary conditions on the magnetic order parameter. This is a different route towards magnetic frustration, which is complementary to the established possibilities due to the local environment of each spin with the negative Toulouse frustration function [46,47] or antiperiodic boundary conditions for the magnetic order parameter [53]. A fingerprint of the competition between different origins of frustrations can be observed in the inhomogeneity of the magnetic order parameter $\boldsymbol{n}$ and local ferrotoroidal response.

We anticipate that our findings can be used to interpret magnetic responses in molecular magnets and complex 3D magnetic architectures fabricated, e.g., by means of glancing angle deposition (GLAD) [11,35,61] or focused electron-beam-induced deposition (FEBID) [15,57]. Furthermore, this theory analysis can be extended to other geometries with specific symmetry properties such as Salkowski curves [42,62] and guide experimental efforts on the design of the sample shapes to realize ferrotoroidal behavior. From the fundamental point of view, we expect that complementary effects may be observed in 3D magnetic nanostructures with constant curvature, where the Dzyaloshinskii vector $\boldsymbol{d}$ is characterized by a nonvanishing binormal component.

In our study, we limit our analysis to the zero-temperature limit. Previous studies indicate that planar ring geometries with the nearest-neighbor exchange support a variety of long-living metastable states at finite temperatures [53]. Furthermore, we note that the intrinsic DMI can contribute to the frustration in quasi-1D systems with interacting spin chains [63]. Epicycles show a similar picture due to a spatially distributed geometry-driven DMI, suggesting the presence of a complex diagram of magnetic states at finite temperatures. This study can be further extended by the analysis of the next-neighbor exchange contributing to the equilibrium states in real systems [64]. These activities can start a new chapter on the thermodynamics of curvilinear magnets, which is yet to be addressed. The effective geometric potential for electrons following curvilinear geometries [65,66] may contribute to the local value of spin-orbit coupling and modify the material parameters, giving rise to more complex spiral states in the vicinity of knots [20,67]. We expect that further modifications of the frustration in curvilinear geometries can be accessed via cross coupling between neighboring parts of the spin chain, such as in the vicinity of knots of the epicycles discussed in this work. Such effect can appear due to the dipolar interaction or randomness of the material parameters enabling next-neighbor coupling at certain distances. Furthermore, the cross coupling could change the topology of the system, leading to the modification of the thermodynamic functions [68–70]. Lattice defects give another degree of freedom to provide noncollinear ground states [54].

ACKNOWLEDGMENTS

We thank Dr. Oleksii M. Volkov (HZDR) and Prof. Denis D. Sheka (Taras Shevchenko National University of Kyiv) for fruitful discussions on curvilinear spin chains. This work is supported in part via German Research Foundation (Grants No. MA5144/22-1, No. MA5144/24-1) and ERC grant 3DmultiFerro (Project No. 101141331). We acknowledge partial support by the Italian Ministry of Foreign Affairs and International Cooperation, Grant No. PGR12351 "ULTRAQMAT." Numerical calculations have been performed using the Hemera high-performance cluster at the HZDR [71].

TABLE I. Parameters used to build epicycles γ_p^r from a spherical curve $\boldsymbol{\beta}$ covering the unit sphere r times and having $|p|$ knots.

Symmetry	r	p	α_1	α_2
C_3	1	-3	$\frac{\pi}{4}$	$\frac{1}{2}\arccos\left(\frac{67-24\sqrt{2}}{71}\right)$
C_4	1	-4	1	0.59973787219

APPENDIX A: GEOMETRY OF EPICYCLES

Here, we follow the procedure described in Bates and Melko [45] to construct spherical epicycles with the given number of knots. The procedure can be briefly summarized as follows. For a given spherical curve $\boldsymbol{\beta} = \{h, k, l\}$ with trigonometric polynomials h, k, and l satisfying $h^2 + k^2 + l^2 = 1$ (i.e., the curve $\boldsymbol{\beta}$ lies on a unit sphere), the epicycle (1) reads

$$x = \frac{1}{\tau}\int_0^s \frac{l\mathrm{d}k - k\mathrm{d}l}{h^2+k^2+l^2},$$
$$y = \frac{1}{\tau}\int_0^s \frac{h\mathrm{d}l - l\mathrm{d}h}{h^2+k^2+l^2},$$
$$z = \frac{1}{\tau}\int_0^s \frac{k\mathrm{d}h - h\mathrm{d}k}{h^2+k^2+l^2}. \tag{A1}$$

A closed curve of constant torsion can be obtained if these polynomials vanish simultaneously being integrated over $[0, 2\pi]$. We can choose a spherical epicycle $\boldsymbol{\beta}$ of the symmetry $C_{|p|}$, which traces the sphere r times and has $|p|$ knots characterized by two geodesic radii $\alpha_{1,2}$. The selection of the geodesic radii should be done in such a way that integrals (A1) vanish. This determines the shape of the respective curve of the constant torsion. The parameters that are used to construct epicycles in our work are shown in Table I. Finally, we rotate the laboratory reference frame to have the $\hat{\boldsymbol{z}}$ axis parallel to the epicycle's axis.

The shape of the curvature $\varkappa$ for the given σ near the maximum can be analytically approximated by a Lorentzian as

$$f(s) = A\,\frac{\Gamma^2}{\Gamma^2 + (s-s_0)^2} + \epsilon, \tag{A2}$$

with A being the amplitude, Γ the half width at half maximum, s_0 the maximum position, and ϵ the offset; see Fig. 1(b). In general, $A \propto \sigma$ and $\Gamma \propto 1/|\sigma|$. The epicycle γ_p^r can be inscribed in a circle of radius $R \propto 1/|\sigma|$.

APPENDIX B: EXCHANGE ENERGY OF A FRUSTRATED SPIN CHAIN

To derive the σ model for curvilinear spin chains with odd number of spins, we follow the procedure for AFM spin chains [48], taking into account the periodic boundary conditions for this geometry. In this case, the exchange part of the Hamiltonian (2) reads

$$\frac{\mathscr{H}_\mathrm{x}}{JS^2} = \frac{1}{2}\sum_{i=1}^{N-1}\big[8m_i^2 + (\Delta\boldsymbol{n}_i)^2 - (\Delta\boldsymbol{m}_i)^2 + 2(\boldsymbol{m}_i\Delta\boldsymbol{n}_{i+1} - \boldsymbol{n}_i\Delta\boldsymbol{m}_{i+1})\big] - 2\big(m_N^2 + 2m_1^2\big) + \boldsymbol{\mu}_0\cdot(\boldsymbol{m}_N + \boldsymbol{m}_1) + \underbrace{\boldsymbol{\mu}_0\cdot(\boldsymbol{n}_1 - \boldsymbol{n}_N)}_{=\delta\mathscr{H}_\mathrm{x}/(JS^2)}. \tag{B1}$$

Here, the sum over i is a source of the expression (3) by the replacement of derivatives $\Delta f_i \to 2af'(s)$ and sums $\sum_i f_i \to 1/(2a)\int f(s)ds$ for a certain energy term f [48]. The last terms outside the summation sign appear due to symmetrization. The last two terms, which are proportional to $\boldsymbol{\mu}_0$, represent the energy of the magnetic defect associated with the unpaired moment. In fact, this defect is virtual because it cannot be associated with a specific lattice site due to the freedom of choice of the spin with $i = 1$ and the respective shift of the origin of the reference frame. In Eq. (B1), the terms outside the sum, which are dependent on $\boldsymbol{m}_1$ and $\boldsymbol{m}_N$, are small for the case of small magnetization and under the assumption that it behaves as a driving variable.

The last term in Eq. (B1) is driven by the primary order parameter. Therefore, it should approach its minimal value in equilibrium. Since the transition to the continuous energy functional is possible for small gradients of $\boldsymbol{n}$ and $a \to 0$, we assume that any small amount of neighboring spins will form a checkerboard order along the certain axis and an inhomogeneity of the magnetic texture can be neglected. Then, $\boldsymbol{n}_1$ and $\boldsymbol{n}_N$ should be either parallel or antiparallel. The requirement that the local spin ordering should be antiferromagnetic everywhere imposes that $\boldsymbol{\mu}_0$ is necessarily antiparallel to both $\boldsymbol{n}_1$ and $\boldsymbol{n}_N$, and thus $\boldsymbol{n}_1$ is co-aligned with $\boldsymbol{n}_N$. Therefore, the continuum Néel vector possesses the antiperiodic boundary conditions $\boldsymbol{n}(0) = -\boldsymbol{n}(L)$.

APPENDIX C: EQUATIONS OF STATE

To describe FM and AFM epicycles with the easy axis of anisotropy ($K > 0$), we use the parametrization (4). The polar and azimuthal angles $\Theta_\mathrm{ea}(\xi)$ and $\Phi_\mathrm{ea}(\xi)$, respectively, are determined by the equations

$$\Theta'' - \sin\Theta\cos\Theta\left[k_{11}(\xi) + \Phi'^2 - (1+k_{33})\cos^2\Phi + \frac{d_\mathrm{B}(\xi)}{2}\Phi' - \frac{d_\mathrm{B}'(\xi)}{4}\sin 2\Phi\right] - k_{13}(\xi)\cos\Phi$$
$$+ \frac{4k_{13}(\xi) - d_\mathrm{B}'(\xi)}{2}\cos^2\Theta\cos\Phi + \frac{1}{2}[d_\mathrm{B}(\xi)\sin\Phi - 2d_\mathrm{T}\cos\Phi]\sin^2\Theta\Phi' = 0,$$
$$\times\sin^2\Theta\Phi'' + \frac{1}{2}\sin\Theta\cos\Theta\{[d_\mathrm{B}(\xi) + 4\Phi']\Theta' + [d_\mathrm{B}'(\xi) - 2k_{13}(\xi)]\sin\Phi\}$$
$$- \frac{\sin^2\Theta}{2}\{[d_\mathrm{B}(\xi)\sin\Phi - 2d_\mathrm{T}\cos\Phi]\Theta' - d_\mathrm{B}'(\xi)\cos^2\Phi + (1+k_{33})\sin 2\Phi\} = 0, \tag{C1}$$

where the subscript "ea" is omitted for simplicity.

To describe FM and AFM epicycles with the hard axis of anisotropy ($K < 0$), we use the parametrization (7). The polar and azimuthal angles $\Theta_{\rm ha}(\xi)$ and $\Phi_{\rm ha}(\xi)$, respectively, are determined by the equations

$$\begin{aligned}
&\Theta'' + \sin\Theta\cos\Theta[1 - k_{33} + k_{11}(\xi)\sin^2\Phi - d_{\rm T}\Phi' - \Phi'^2] + k_{13}(\xi)\sin\Phi \\
&+ \{d_{\rm B}(\xi)\cos\Phi\Phi' + [d'_{\rm B}(\xi) - 4k_{13}(\xi) - d_{\rm B}\Phi']\sin\Phi\}\frac{\sin^2\Theta}{2} = 0, \\
&\times \sin^2\Theta\Phi'' + \sin\Theta\cos\Theta\left[k_{13}(\xi)\cos\Phi + d_{\rm T}\Theta' + 2\Theta'\Phi' - \frac{d'_{\rm B}(\xi)}{2}\sin\Phi\right] \\
&+ \frac{\sin^2\Theta}{2}[d_{\rm B}(\xi)(\sin\Phi - \cos\Phi)\Theta' + k_{11}(\xi)\sin 2\Phi] = 0,
\end{aligned} \tag{C2}$$

where the subscript "ha" is omitted for simplicity.

APPENDIX D: SPIN-LATTICE SIMULATIONS

To analyze magnetic spin chains numerically, we solve the Landau-Lifshitz-Gilbert equation

$$\frac{d\boldsymbol{\mu}_i}{dt} = \frac{1}{\hbar S}\boldsymbol{\mu}_i \times \frac{\partial \mathscr{H}}{\partial \boldsymbol{\mu}_i} + \alpha_{\rm G}\boldsymbol{\mu}_i \times \frac{d\boldsymbol{\mu}_i}{dt}, \quad i = \overline{1, N}, \tag{D1}$$

using the in-house-developed spin-lattice simulation suite SLASI [72] with the midpoint integration scheme. Here, t is time, $\hbar$ is the reduced Planck constant, and $\alpha_{\rm G}$ is the Gilbert damping parameter. By choosing a certain initial state, we solve Eq. (D1) until the energy reaches a constant level. Then, we compare the energies of states obtained from different initial configurations and select the one which has the lowest energy. For all simulations, we choose scales between J, $\mathcal{K}$, and $\mu_{\rm B}$ in such a way as to have $\ell/a = 10$. The value of magnetic length ℓ is calculated based on the effective anisotropy stemming from the dipolar interaction for the given sign of J; see Sec. III C for details.

For simulations of magnetically soft systems, we set $\mathcal{K} = 0$. For simulations of magnetically hard systems, $\boldsymbol{H}_{\rm d} \equiv 0$ is imposed. The numerical procedure to determine the ground states is as follows. By choosing one of the predefined initial magnetic textures, the system is relaxed by solving Eq. (D1). The total time of relaxation for the majority of simulations is $t_{\max} \approx 174\hbar S/\mathcal{K}$ with the integration step $\Delta t \approx 0.000\,174\hbar S/\mathcal{K}$. In some cases, the simulation time is extended up to $870\hbar S/\mathcal{K}$. The sets of initial states for all studied systems include the orientation of $\boldsymbol{n}$ along $\pm\hat{\boldsymbol{x}}$, $\pm\hat{\boldsymbol{y}}$, $\pm\hat{\boldsymbol{z}}$, $\pm\boldsymbol{e}_{\rm T}$, $\pm\boldsymbol{e}_{\rm N}$, $\pm\boldsymbol{e}_{\rm B}$ and several runs from different random states. To get the lowest-energy states for hard-axis AFM and frustrated epicycles, additional initial states with $\Theta_{\rm ini} = \pi/2$ and piecewise profiles of $\Phi_{\rm ini}$ close to the final state are used.

The discrete Frenet-Serret basis $\{\boldsymbol{e}_{\rm T}, \boldsymbol{e}_{\rm N}, \boldsymbol{e}_{\rm B}\}$ is calculated based on the shape of $\boldsymbol{\gamma}$ [73], which is numerically determined with a step much finer than the intersite distance a. We note that for the chosen ℓ/a ratio, the same procedure can be applied to the set of magnetic lattice sites, while the discreteness effects are still negligibly small.

To check the critical torsion at which the ground state is changed, we performed a series of simulations of the easy-axis FM epicycles γ^1_{-3} for different σ, where the initial states are selected to be along $\boldsymbol{e}_{\rm T}$ and along the axis of symmetry of the epicycle. While all states remain similar visually, at $\sigma_{\rm cr} = 0.377 \pm 0.016$ there is a change of the spatial distribution of $\Phi_{\rm ea}$. For $\sigma < \sigma_{\rm cr}$, the azimuthal angle behaves qualitatively similar to the picture shown in Fig. 2(b) with $\max|\Phi_{\rm ea}| \sim 0.1\pi$. For $\sigma > \sigma_{\rm cr}$, there is a continuous change of Φ by 6π at $0 \leqslant \xi < X$, which is an indication of the difference in topology of magnetic states because of the helimagnetic transition due to a strong curvature-induced DMI [17].

[1] P. Gentile, M. Cuoco, O. M. Volkov, Z.-J. Ying, I. J. Vera-Marun, D. Makarov, and C. Ortix, Electronic materials with nanoscale curved geometries, Nat. Electron. **5**, 551 (2022).

[2] M. Vozmediano, M. Katsnelson, and F. Guinea, Gauge fields in graphene, Phys. Rep. **496**, 109 (2010).

[3] A. G. Grushin, J. W. F. Venderbos, A. Vishwanath, and R. Ilan, Inhomogeneous Weyl and Dirac semimetals: Transport in axial magnetic fields and Fermi arc surface states from pseudo-Landau levels, Phys. Rev. X **6**, 041046 (2016).

[4] V. M. Fomin and O. V. Dobrovolskiy, A perspective on superconductivity in curved 3D nanoarchitectures, Appl. Phys. Lett. **120**, 090501 (2022).

[5] D. Makarov, O. M. Volkov, A. Kákay, O. V. Pylypovskyi, B. Budinská, and O. V. Dobrovolskiy, New dimension in magnetism and superconductivity: 3D and curvilinear nanoarchitectures, Adv. Mater. **34**, 2101758 (2022).

[6] D. Raftrey, A. Hierro-Rodriguez, A. Fernandez-Pacheco, and P. Fischer, The road to 3-dim nanomagnetism: Steep curves and architectured crosswalks, J. Magn. Magn. Mater. **563**, 169899 (2022).

[7] *Curvilinear Micromagnetism*, edited by D. Makarov and D. D. Sheka (Springer International, Cham, 2022).

[8] D. D. Sheka, O. V. Pylypovskyi, O. M. Volkov, K. V. Yershov, V. P. Kravchuk, and D. Makarov, Fundamentals of curvilinear ferromagnetism: Statics and dynamics of geometrically curved wires and narrow ribbons, Small **18**, 2105219 (2022).

[9] C. Ortix and J. van den Brink, Magnetoelectricity induced by rippling of magnetic nanomembranes and wires, Phys. Rev. Res. **5**, L022063 (2023).

[10] M. Fiebig, T. Lottermoser, D. Meier, and M. Trassin, The evolution of multiferroics, Nat. Rev. Mater. **1**, 16046 (2016).

[11] C. Phatak, Y. Liu, E. B. Gulsoy, D. Schmidt, E. Franke-Schubert, and A. Petford-Long, Visualization of the magnetic structure of sculpted three-dimensional cobalt nanospirals, Nano Lett. **14**, 759 (2014).

[12] V. Magdanz, M. Medina-Sánchez, L. Schwarz, H. Xu, J. Elgeti, and O. G. Schmidt, Spermatozoa as functional components of robotic microswimmers, Adv. Mater. **29**, 1606301 (2017).

[13] D. Y. Nam, A. Y. Samardak, Y. S. Jeon, S. H. Kim, A. V. Davydenko, A. V. Ognev, A. S. Samardak, and Y. K. Kim, Magnetization reversal of ferromagnetic nanosprings affected by helical shape, Nanoscale **10**, 20405 (2018).

[14] D. Sanz-Hernández, A. Hierro-Rodriguez, C. Donnelly, J. Pablo-Navarro, A. Sorrentino, E. Pereiro, C. Magén, S. McVitie, J. M. de Teresa, S. Ferrer, P. Fischer, and A. Fernández-Pacheco, Artificial double-helix for geometrical control of magnetic chirality, ACS Nano **14**, 8084 (2020).

[15] C. Phatak, C. S. Miller, Z. Thompson, E. B. Gulsoy, and A. K. Petford-Long, Curved three-dimensional cobalt nanohelices for use in domain wall device applications, ACS Appl. Nano Mater. **3**, 6009 (2020).

[16] J. Fullerton, A. R. C. McCray, A. K. Petford-Long, and C. Phatak, Understanding the effect of curvature on the magnetization reversal of three-dimensional nanohelices, Nano Lett. **24**, 2481 (2024).

[17] D. D. Sheka, V. P. Kravchuk, K. V. Yershov, and Y. Gaididei, Torsion-induced effects in magnetic nanowires, Phys. Rev. B **92**, 054417 (2015).

[18] O. V. Pylypovskyi, D. D. Sheka, V. P. Kravchuk, K. V. Yershov, D. Makarov, and Y. Gaididei, Rashba torque driven domain wall motion in magnetic helices, Sci. Rep. **6**, 23316 (2016).

[19] K. V. Yershov, V. P. Kravchuk, D. D. Sheka, and Y. Gaididei, Curvature and torsion effects in spin-current driven domain wall motion, Phys. Rev. B **93**, 094418 (2016).

[20] O. M. Volkov, D. D. Sheka, Y. Gaididei, V. P. Kravchuk, U. K. Rößler, J. Fassbender, and D. Makarov, Mesoscale Dzyaloshinskii-Moriya interaction: Geometrical tailoring of the magnetochirality, Sci. Rep. **8**, 866 (2018).

[21] O. Volkov, U. K. Rossler, J. Fassbender, and D. Makarov, Concept of artificial magnetoelectric materials via geometrically controlling curvilinear helimagnets, J. Phys. D **52**, 345001 (2019).

[22] T. Salamone, H. G. Hugdal, M. Amundsen, and S. H. Jacobsen, Electrical control of superconducting spin valves using ferromagnetic helices, Appl. Phys. Lett. **125**, 062602 (2024).

[23] D. Das Gupta and S. K. Maiti, Antiferromagnetic helix as an efficient spin polarizer: Interplay between electric field and higher-order hopping, Phys. Rev. B **106**, 125420 (2022).

[24] K. Mondal, S. Ganguly, and S. K. Maiti, Thermoelectric phenomena in an antiferromagnetic helix: Role of electric field, Phys. Rev. B **108**, 195401 (2023).

[25] D. Das Gupta and S. K. Maiti, Spin current rectification in a helical magnetic system with vanishing net magnetization, Ann. Phys. **454**, 169343 (2023).

[26] R. Moreno, V. L. Carvalho-Santos, A. P. Espejo, D. Laroze, O. Chubykalo-Fesenko, and D. Altbir, Oscillatory behavior of the domain wall dynamics in a curved cylindrical magnetic nanowire, Phys. Rev. B **96**, 184401 (2017).

[27] G. H. R. Bittencourt, V. L. Carvalho-Santos, O. Chubykalo-Fesenko, D. Altbir, and R. Moreno, Dynamics of chiral domain walls in bent cylindrical magnetic nanowires, J. Appl. Phys. **135**, 063906 (2024).

[28] O. M. Volkov, A. Kákay, F. Kronast, I. Mönch, M.-A. Mawass, J. Fassbender, and D. Makarov, Experimental observation of exchange-driven chiral effects in curvilinear magnetism, Phys. Rev. Lett. **123**, 077201 (2019).

[29] O. M. Volkov, F. Kronast, I. Mönch, M.-A. Mawass, A. Kákay, J. Fassbender, and D. Makarov, Experimental and theoretical study of curvature effects in parabolic nanostripes, Phys. Stat. Sol. (RRL) **13**, 1800309 (2019).

[30] K. V. Yershov, Dynamics of domain walls in curved antiferromagnetic wires, Phys. Rev. B **105**, 064407 (2022).

[31] G. H. R. Bittencourt, S. Castillo-Sepúlveda, O. Chubykalo-Fesenko, R. Moreno, D. Altbir, and V. L. Carvalho-Santos, Domain wall damped harmonic oscillations induced by curvature gradients in elliptical magnetic nanowires, Phys. Rev. B **106**, 174424 (2022).

[32] K. V. Yershov, V. P. Kravchuk, D. D. Sheka, O. V. Pylypovskyi, D. Makarov, and Y. Gaididei, Geometry-induced motion of magnetic domain walls in curved nanostripes, Phys. Rev. B **98**, 060409(R) (2018).

[33] G. H. R. Bittencourt, O. Chubykalo-Fesenko, D. Altbir, V. L. Carvalho-Santos, and R. Moreno, Area law for magnetic domain walls in bent cylindrical nanowires, Phys. Rev. B **106**, 094410 (2022).

[34] H. Zhao, R. Cheng, and Q.-H. Liu, Long range motion of domain wall in antiferromagnetic 3D curved nanowire, Results Phys. **52**, 106848 (2023).

[35] J. Askey, M. O. Hunt, L. Payne, A. van den Berg, I. Pitsios, A. Hejazi, W. Langbein, and S. Ladak, Direct visualization of domain wall pinning in sub-100 nm 3D magnetic nanowires with cross-sectional curvature, Nanoscale **16**, 17793 (2024).

[36] L. Bogani and W. Wernsdorfer, Molecular spintronics using single-molecule magnets, Nat. Mater. **7**, 179 (2008).

[37] L. Ungur, S.-Y. Lin, J. Tang, and L. F. Chibotaru, Single-molecule toroics in Ising-type lanthanide molecular clusters, Chem. Soc. Rev. **43**, 6894 (2014).

[38] *Single Molecule Toroics*, edited by K. Murray (Springer International, Cham, 2022).

[39] O. V. Pylypovskyi, V. P. Kravchuk, D. D. Sheka, D. Makarov, O. G. Schmidt, and Y. Gaididei, Coupling of chiralities in spin and physical spaces: The Möbius ring as a case study, Phys. Rev. Lett. **114**, 197204 (2015).

[40] Y. Gaididei, A. Goussev, V. P. Kravchuk, O. V. Pylypovskyi, J. M. Robbins, D. Sheka, V. Slastikov, and S. Vasylkevych, Magnetization in narrow ribbons: Curvature effects, J. Phys. A: Math. Theor. **50**, 385401 (2017).

[41] A. Calini and T. Ivey, Bäcklund transformations and knots of constant torsion, J. Knot Theor. Ramific. **07**, 719 (1998).

[42] J. Monterde, Salkowski curves revisited: A family of curves with constant curvature and non-constant torsion, Comput. Aid. Geometr. Design **26**, 271 (2009).

[43] G. Koenigs, On the shape of constant torsion curves, Annal. Facult. Sci. Toulouse Math. **1**, E1 (1887).

[44] J. L. Weiner, Closed curves of constant torsion. II, Proc. Am. Math. Soc. **67**, 306 (1977).

[45] L. M. Bates and O. M. Melko, On curves of constant torsion I, J. Geom. **104**, 213 (2013).

[46] G. Toulouse, Theory of the frustration effect in spin glasses. I, Commun. Phys. **2**, 115 (1977).

[47] G. Toulouse, Spin glasses with special emphasis on frustration effects, in *Lecture Notes in Physics*, edited by C. Castellani, C. Di Castro, and L. Peliti (Springer, Berlin, 1981), pp. 166–173.

[48] O. V. Pylypovskyi, Y. A. Borysenko, J. Fassbender, D. D. Sheka, and D. Makarov, Curvature-driven homogeneous Dzyaloshinskii-Moriya interaction and emergent weak ferromagnetism in anisotropic antiferromagnetic spin chains, Appl. Phys. Lett. **118**, 182405 (2021).

[49] O. V. Pylypovskyi, D. Y. Kononenko, K. V. Yershov, U. K. Rößler, A. V. Tomilo, J. Fassbender, J. van den Brink, D. Makarov, and D. D. Sheka, Curvilinear one-dimensional antiferromagnets, Nano Lett. **20**, 8157 (2020).

[50] A. Aharoni, *Introduction to the Theory of Ferromagnetism* (Oxford University Press, Oxford, 1996).

[51] O. V. Pylypovskyi, A. V. Tomilo, D. D. Sheka, J. Fassbender, and D. Makarov, Boundary conditions for the Néel order parameter in a chiral antiferromagnetic slab, Phys. Rev. B **103**, 134413 (2021).

[52] Y. A. Borysenko, D. D. Sheka, J. Fassbender, J. van den Brink, D. Makarov, and O. V. Pylypovskyi, Field-induced spin reorientation transitions in antiferromagnetic ring-shaped spin chains, Phys. Rev. B **106**, 174426 (2022).

[53] S. Castillo-Sepúlveda, R. A. Escobar, D. Altbir, M. Krizanac, and E. Y. Vedmedenko, Magnetic Möbius stripe without frustration: Noncollinear metastable states, Phys. Rev. B **96**, 024426 (2017).

[54] O. Cador, D. Gatteschi, R. Sessoli, F. K. Larsen, J. Overgaard, A.-L. Barra, S. J. Teat, G. A. Timco, and R. E. P. Winpenny, The magnetic Möbius strip: Synthesis, structure, and magnetic studies of odd-numbered antiferromagnetically coupled wheels, Angew. Chem. Intl. Ed. **43**, 5196 (2004).

[55] M. L. Baker, O. Waldmann, S. Piligkos, R. Bircher, O. Cador, S. Carretta, D. Collison, F. Fernandez-Alonso, E. J. L. McInnes, H. Mutka, A. Podlesnyak, F. Tuna, S. Ochsenbein, R. Sessoli, A. Sieber, G. A. Timco, H. Weihe, H. U. Güdel, and R. E. P. Winpenny, Inelastic neutron scattering studies on the odd-membered antiferromagnetic wheel Cr_8Ni, Phys. Rev. B **86**, 064405 (2012).

[56] L. O'Brien, D. Petit, E. R. Lewis, R. P. Cowburn, D. E. Read, J. Sampaio, H. T. Zeng, and A.-V. Jausovec, Tunable remote pinning of domain walls in magnetic nanowires, Phys. Rev. Lett. **106**, 087204 (2011).

[57] C. Donnelly, A. Hierro-Rodríguez, C. Abert, K. Witte, L. Skoric, D. Sanz-Hernández, S. Finizio, F. Meng, S. McVitie, J. Raabe, D. Suess, R. Cowburn, and A. Fernández-Pacheco, Complex free-space magnetic field textures induced by three-dimensional magnetic nanostructures, Nat. Nanotechnol. **17**, 136 (2022).

[58] D. D. Sheka, V. P. Kravchuk, and Y. Gaididei, Curvature effects in statics and dynamics of low dimensional magnets, J. Phys. A: Math. Theor. **48**, 125202 (2015).

[59] N. A. Spaldin, M. Fechner, E. Bousquet, A. Balatsky, and L. Nordström, Monopole-based formalism for the diagonal magnetoelectric response, Phys. Rev. B **88**, 094429 (2013).

[60] S. Bhowal and N. A. Spaldin, Magnetoelectric classification of skyrmions, Phys. Rev. Lett. **128**, 227204 (2022).

[61] J. G. Gibbs, A. G. Mark, T.-C. Lee, S. Eslami, D. Schamel, and P. Fischer, Nanohelices by shadow growth, Nanoscale **6**, 9457 (2014).

[62] J. Monterde, Salkowski curves and spherical epicycloids, J. Geom. **115**, 31 (2024).

[63] M. Hälg, W. E. A. Lorenz, K. Y. Povarov, M. Månsson, Y. Skourski, and A. Zheludev, Quantum spin chains with frustration due to Dzyaloshinskii-Moriya interactions, Phys. Rev. B **90**, 174413 (2014).

[64] K. Maisinger and U. Schollwöck, Thermodynamics of frustrated quantum spin chains, Phys. Rev. Lett. **81**, 445 (1998).

[65] L. I. Magarill, A. V. Chaplik, and M. V. Entin, Spectrum and kinetics of electrons in curved nanostructures, Phys. Usp. **48**, 953 (2005).

[66] P. Gentile, M. Cuoco, and C. Ortix, Curvature-induced Rashba spin-orbit interaction in strain-driven nanostructures, SPIN **03**, 1340002 (2013).

[67] A. Edström, D. Amoroso, S. Picozzi, P. Barone, and M. Stengel, Curved magnetism in CrI_3, Phys. Rev. Lett. **128**, 177202 (2022).

[68] K. Kaneda and Y. Okabe, Finite-size scaling for the Ising model on the Möbius strip and the Klein bottle, Phys. Rev. Lett. **86**, 2134 (2001).

[69] O. A. Vasilyev, A. Maciołek, and S. Dietrich, Criticality senses topology, Europhys. Lett. **128**, 20002 (2019).

[70] O. A. Vasilyev, A. Maciołek, and S. Dietrich, Sensitivity of the thermodynamics of two-dimensional systems towards the topological classes of their surfaces, Physica A **624**, 128960 (2023).

[71] High Performance Computing at Helmholtz-Zentrum Dresden-Rossendorf (2024), http://www.hzdr.de.

[72] SLaSi spin-lattice simulations package, http://slasi.knu.ua/.

[73] S. Hu, M. Lundgren, and A. J. Niemi, Discrete Frenet frame, inflection point solitons, and curve visualization with applications to folded proteins, Phys. Rev. E **83**, 061908 (2011).